Nature Communications

https://doi.org/10.1038/s41467-026-68348-w

Article in Press

Sequence-encoded layered heteroleptic metalla-[2]catenanes for programmable supramolecular function

Received: 24 September 2025

Accepted: 24 December 2025

Cite this article as: Zhang, Y.-W., Zhang, H.-N., Wang, M.-X. *et al.* Sequence-encoded layered heteroleptic metalla-[2]catenanes for programmable supramolecular function. *Nat Commun* (2026). https://doi.org/10.1038/s41467-026-68348-w

Ya-Wen Zhang, Hai-Ning Zhang, Ming-Xia Wang, Xin Li & Ying-Feng Han

Sequence-Encoded Layered Heteroleptic Metalla-[2]catenanes for Programmable Supramolecular Function

Ya-Wen Zhang[1,§], Hai-Ning Zhang[2,§], Ming-Xia Wang[1], Xin Li[1] & Ying-Feng Han[1,*]

[1]College of Chemistry and Materials Science, Northwest University, Xi'an, 710127, P. R. China.

[2]College of Chemistry, Zhengzhou University, Zhengzhou, 450001, P. R. China.

[§]These authors contributed equally.

*Corresponding author: *Prof.* Y.-F. Han; E-mail address: yfhan@nwu.edu.cn.

Abstract: Molecular information encoded within supramolecular frameworks offers a powerful paradigm for directing emergent function beyond the genetic code, but systematic investigations into alternative spatial configurations and their consequences remain scarce. Here we use metalla-[2]catenanes to probe sequence–function relationships in layered architectures. By combining two or three size-matched N-heterocyclic carbene ligands with Ag(I) nodes, we selectively construct heteroleptic metalla-[2]catenanes through both direct assembly and supramolecular fusion pathways. X-ray crystallographic analysis unambiguously confirms the targeted sequences, while semiempirical and density functional theory calculations reveal their thermodynamic preference over alternative isomers. Photothermal conversion studies further demonstrate that sequence-specific charge-transfer interactions yield distinct macroscopic responses. Collectively, these results identify heteroleptic metalla-[2]catenanes as a robust model for elucidating how spatial arrangement governs system-level behavior and for advancing molecular coding principles in functional supramolecular design.

Introduction

Molecular information is emerging as a transformative paradigm that extends far beyond the genetic code of nucleic acids[1]. Information can be encoded within molecular frameworks that have distinct structural and chemical features, redefining how it is stored, processed, and transmitted at the molecular level[2,3]. In self-assembly, the spatial arrangement of functional motifs acts as a "molecular code" that dictates intermolecular interactions, symmetry, and dynamic response pathways, ultimately directing emergent function[4–8]. These principles provide a powerful foundation for the bottom-up design of advanced functional materials, with numerous implications for biomimetic manufacturing[9,10], energy conversion[11], and chiral technologies[12,13].

Despite these advancements, establishing precise structure–function relationships between the sequence of functional motifs at the molecular level and the macroscopic properties of assembled systems remains a central challenge[14–16]. Current research on the controllable design of assemblies with specific motif sequences remains limited. To address this issue, recent efforts have focused on the development of multicomponent self-assembly systems incorporating diverse motifs[17–19]. In metallosupramolecular assemblies, synthetic chemists have achieved nonstatistical precision[8,20–22] in multicomponent architectures—overcoming entropy barriers, avoiding self-sorting, and suppressing statistical mixtures—through strategies such as guest templation[23,24], geometric complementarity[25,26], coordination-site engineering[27–31], hierarchical assembly[32,33], and kinetic control[34–36]. Nevertheless, most studies have focused on cavity-centered functions, arising from the anisotropic radial (Fig. 1a, for metallocages) or circular arrangement (Fig. 1b, for metallacycles) of motifs, particularly in recognition[37,38] and confined catalysis[33,39–42]. In contrast, systematic investigations into alternative spatial organizations—such as layered or planar grid arrangements—and their effect on properties (Fig. 1c), including electron transport, optical behavior, and mechanical performance, remain scarce. There is therefore an urgent need to construct self-assembly systems with spatial configurations beyond radial architectures to determine how specific motif arrangements translate into system-level functions.

Building on the previous work with metal N-heterocyclic carbene (NHC) assemblies[43–46], we

identified tetranuclear metalla-[2]catenane (MCAT) as an ideal platform for this purpose[47,48]. Unlike conventional metallocages and metallacycles featuring radial arrangements, the four NHC ligands in MCAT use a distinctive stereoscopic layered configuration. Heteroleptic assembly of two or three size-matched NHC ligands with four Ag(I) nodes can theoretically yield MCATs with 8 and 18 possible outcome sequences (Fig. 1d and 1e), respectively, providing a versatile platform to probe stereoscopic, layered sequence–function relationships.

In this study, we report the selective construction of three heteroleptic MCATs with integrative self-sorting behavior, including two distinct two-component sequences and one three-component sequence. These assemblies were accessed either via direct assembly of NHC ligands with Ag(I) nodes or structural transformation from homoleptic precursors trough a supramolecular fusion strategy. All the structures were unambiguously confirmed by single-crystal X-ray diffraction and high-resolution mass spectrometry. Complementary theoretical calculation studies that combine semiempirical methods and density functional theory (DFT) calculations revealed that the binding energies of the observed MCATs are significantly lower than those of their respective isomers, supporting the thermodynamic preference for the obtained structures. Furthermore, photothermal conversion experiments demonstrated sequence-dependent differences in performance, which can be attributed to charge-transfer interactions between the distinct functional motifs. Collectively, these findings establish heteroleptic MCATs as a versatile platform for probing the relationship between spatial motif arrangement and macroscopic function in multicomponent assemblies. This approach provides new insights into how molecular coding principles can be applied to the design of functional supramolecular systems.

Results

Synthesis and characterization of homoleptic $MCAT_{AAAA}$ and MC_{BB}

Imidazo[1,5-*a*]pyridinium salts H_2A and H_2B were prepared in four steps from 2,7-dibromophenazine and 2,6-dibromoanthracene by adjusting the reported procedure[49]. The complete synthetic route is outlined in the Supplementary Information (Supplementary Figs. 1–26). The imidazo[1,5-*a*]pyridine-based NHC ligands were strategically chosen to fulfill the

structural requirement for optimal interplanar surface-to-surface separation (~6.6 Å), facilitating the directional assembly of mechanically interlocked supramolecular architectures through precise π-system alignment[47–49]. The homoleptic $MCAT_{AAAA}$ was obtained in 93% yield via the reaction of H_2A with excess Ag_2O in acetonitrile under the exclusion of light at 65°C for 12 h (Fig. 2, method a). The formation was verified by two-dimensional (2D) NMR spectroscopy and ESI mass spectrometry (Supplementary Figs. 27–32) as follows: Peaks in the ^1H NMR spectrum of $MCAT_{AAAA}$ (Supplementary Fig. 27) showed distinct shifts and were split into two sets of signals, revealing the presence of two chemically inequivalent di-NHC ligands within the assembly. As expected for Ag^I–NHC [2]catenane, two di-NHC ligands are located inside the cavity, and the remaining ligands constitute the outer framework. The formation of $MCAT_{AAAA}$ was also evident from $^{13}C\{^1H\}$ NMR spectroscopy showing the two well-resolved sets of carbon signals (Supplementary Fig. 28). The ^1H diffusion-ordered spectroscopy (DOSY) NMR spectrum of $MCAT_{AAAA}$ showed a single diffusion coefficient ($D = 5.01 \times 10^{-10}$ m^2 s^{-1}) for all of the aromatic proton signals, suggesting that all the resonances belong to a single assembly (Supplementary Fig. 31). ESI mass measurements also indicated the [2]catenane structure of $MCAT_{AAAA}$, with prominent peaks at m/z = 891.5664 (calcd for $[MCAT_{AAAA} - 3(PF_6^-)]^{3+}$ 891.5541) and 1409.8347 (calcd for $[MCAT_{AAAA} - 2(PF_6^-)]^{2+}$ 1409.8134) (Supplementary Fig. 32), which was consistent with the theoretical distribution.

The single-crystal X-ray diffraction (SCXRD) structure of $MCAT_{AAAA}$ is shown in Fig. 3a. The two identical binuclear MR_{AA}s are interlocked, constituting a Hopf link topology. SCXRD analysis revealed efficient π···π stacking interactions between the four phenazine rings, as inferred from the centroid−centroid separations of 3.4, 3.3, and 3.4 Å between adjacent phenazine planes. These interactions are the main driving forces for the formation of the interlocked structure. In addition, there is a crossing angle of ca. 85° between the two “inner” phenazine rings, whereas the “outer” adjacent pairwise phenazine rings are nearly parallel.

However, when H_2B (with anthracene replaced by phenazine in H_2A) was treated with Ag_2O under the same conditions as described for the assembly of $MCAT_{AAAA}$, only the simple binuclear

MR_{BB} was isolated rather than an interlocking topology (Fig. 2, method b). The MR_{BB} was identified by NMR spectroscopy and ESI mass (Supplementary Figs. 33–37). The single resonance pattern (rather than the common doublet signals of interlocked topologies[47,49]) of the ^{1}H (Supplementary Fig. 33) and $^{13}C\{^{1}H\}$ (Supplementary Fig. 34) NMR spectra of the resulting assembly suggested a simpler topology. Moreover, the ^{1}H DOSY spectrum (Supplementary Fig. 36) as well as the ESI mass spectrum (Supplementary Fig. 37) also confirm the formation of MR_{BB} (*m/z* = 630.1871, calcd. for $[MR_{BB} - 2(PF_6^-)]^{2+}$ 630.1832). These results indicate that compared with purely hydrocarbon-based aromatic groups, heteroaromatic groups have greater advantages in the construction of interlocked topologies[50].

Synthesis and characterization of heteroleptic MCATs with two different di-NHC ligands

Inspired by previous work[51], we realized that the charge-transfer interaction between two NHC ligands with similar sizes and opposite electronic centers facilitates the formation of heteroleptic Ag^{I}-NHC assemblies while inhibiting the formation of homoleptic Ag^{I}–NHC assemblies. Thus, we employed a similar strategy to construct two-component MCATs.

First, we attempted to assemble the system by reacting imidazo[1,5-α]pyridinium salts H_2A and H_2B in a 1:1 molar ratio with a slight excess of Ag_2O. Subsequent ^{1}H NMR spectroscopy (Supplementary Fig. 38) revealed that assembly in the presence of two imidazo[1,5-α]pyridinium salts and Ag^{I} ions failed to yield a single product. Mass spectrometry (Supplementary Fig. 39) indicated the presence of peaks corresponding not only to MR_{BB} but also to a heteroleptic MCAT, where the ratio of NHC ligands A to B was 3:1. Although we obtained single crystals of MCAT via vapor diffusion, X-ray crystallography confirmed that the structure was only an MCAT formed by the catenation of two MRs (Supplementary Fig. 40). Owing to the similar scattering factors of carbon (C) and nitrogen (N) atoms, the specific arrangement of the ligands could not be definitively assigned. Consequently, we speculated that the products included MR_{BB} with a mixture of possibly $MCAT_{ABAA}$ and $MCAT_{BAAA}$. To avoid this issue, we considered introducing the NHC ligand C, which has a similar size but an opposite charge center. This ligand was previously shown to enable the high-yield construction of homoleptic $MCAT_{CCCC}$ with Ag^{I} (Fig. 2, method c). Considering the

electron-donating central core of the proligand H_2C, when it is strategically assembled with a di-NHC ligand containing an electron-deficient aromatic scaffold in the presence of Ag_2O as a metallic precursor, it may facilitate the creation of a new heteroleptic MACT system. This architecture is anticipated to exhibit increased thermodynamic stability and structural complexity, guided by complementary electronic interactions between the donor–acceptor pair and the directional coordination preferences of the Ag^I nodes.

To test this hypothesis, heating a mixture of H_2A and H_2C in a ratio of 1:1 with a slight excess of Ag_2O in acetonitrile indeed resulted in the exclusive formation of heteroleptic [2]catenane with a yield of 92% (Fig. 2, *method* d). With the slow diffusion of diethyl ether into the acetonitrile solution at ambient temperature, yellow block crystals suitable for SCXRD were obtained. Structural analysis of single crystals unambiguously established the composition and molecular structure of this heteroleptic MCAT with a sequence of CAAC (Fig. 3b). Inspection of the structure reveals that every silver(I) ion simultaneously coordinates NHC ligands A and C linearly to create two heteroleptic $MR_{AC}S$, which are further interlocked via mechanical bonds to form heteroleptic $MCAT_{CAAC}$. This arrangement results in extensive π···π stacking between the ligand backbones, which are arranged into pyrene–phenazine–phenazine–pyrene stacks with distances of ca. 3.3–3.4 Å between the mean planes of the stacked rings. Interestingly, the selective formation of this heteroleptic MCAT structure with a donor–acceptor–acceptor–donor stack provides a compelling depiction of intramolecular self-sorting that differs from the commonly accepted self-sorting, in which donor and acceptor aromatic moieties are arranged into complementary alternating stacks that are generally regarded as the most favorable arrangement for providing optimum electronic overlap.

After the solid-state molecular structure of $MCAT_{CAAC}$ was determined, relevant NMR spectroscopic experiments performed to further explore its behavior in solution (Supplementary Figs. 41–45). With the ^1H NMR spectra of ligand precursors H_2A (Fig. 4a) and H_2C (Fig. 4c) and the 2D NMR spectra of $MCAT_{CAAC}$, the peaks in the ^1H NMR spectrum of $MCAT_{CAAC}$ can be clearly identified (Fig. 4d and Supplementary Fig. 41) and are consistent with the characterization

of the heteroleptic metalla[2]catenane structure. The ^{1}H NMR spectrum of $MCAT_{CAAC}$ (Fig. 4d) shows one set of signals that are equally integrated for each ligand. The total amount of 15 aromatic signals indicated that each ligand maintained its twofold symmetry in the interlocked assembly. Strongly upfield-shifted resonances were observed for the aromatic protons of the phenazine units H9', H13' and H10' (δ = 7.33, 6.74 and 6.66 ppm, respectively), whereas the proton resonances for the pyrene groups H13, H14 and H11 were recorded at δ = 7.81, 7.70 and 7.36 ppm (Fig. 4d), which were attributed to the shielded surroundings inside the cavity of the interlocked architectures. In addition, the ^{1}H DOSY NMR spectrum of $MCAT_{CAAC}$ revealed that only one diffusion coefficient D (5.50×10^{-10} m^2 s^{-1}) (Supplementary Fig. 45), suggesting that only one stoichiometric group of the assembly formed.

Additionally, the assembly of $MCAT_{CAAC}$ in solution was further confirmed by ESI mass data (Fig. 4g and Supplementary Fig. 46). Prominent peaks at m/z = 906.2563 (calcd for $[MCAT_{CAAC} - 3(PF_6^-)]^{3+}$ 906.2271) and 1431.8179 (calcd for $[MCAT_{CAAC} - 2(PF_6^-)]^{2+}$ 1431.8231) were observed, which closely matched the anticipated theoretical distributions.

We subsequently examined the combination of H_2B and H_2C at a ratio of 1:1 with Ag_2O under the same conditions as described for the assembly of $MCAT_{CAAC}$, which resulted in the formation of heteroleptic $MCAT_{CBBC}$ with a yield of 90% (Fig. 2, method e). Single crystals of $MCAT_{CBBC}$ were obtained by slow diffusion of diethyl ether into an acetonitrile solution of the assembly. SCXRD analysis (Fig. 3c) confirmed that the molecular structure of $MCAT_{CBBC}$ closely resembled that of $MCAT_{CAAC}$, where two identical heteroleptic MR interpenetrate to form the heteroleptic MCAT. Moreover, each independent MR is composed of di-NHC ligands B and C, as well as two silver ions. Like the $MCAT_{CAAC}$ assembly, the pyrene-bridged ligand C was located at the top and bottom, whereas the anthracene-bridged ligand B was located in the middle of the $MCAT_{CBBC}$ assembly. Triple typical π···π stacking interactions were also observed between the ligand backbones, which are arranged into pyrene–anthracene–anthracene–pyrene stacks with distances of approximately 3.5 Å between the mean planes of the stacked rings.

Like assembly $MCAT_{CAAC}$, the structure of the heteroleptic $MCAT_{CBBC}$ in solution was also

investigated (Supplementary Figs. 51–56). Consistent with expectations, the ^{1}H NMR analysis of $MCAT_{CBBC}$ (Fig. 4e and Supplementary Fig. 51) confirmed the equimolar presence of ligand precursors H_2B and H_2C (1:1 ratio). In addition, strongly upfield-shifted resonances were also observed for the aromatic protons of the anthracene units H9', H13', H10' and H14' (δ = 6.91, 6.59, 6.52 and 4.95 ppm, respectively), whereas the proton resonances for the pyrene groups H13, H14, H11 and H10 were recorded at δ = 7.77, 7.69, 7.27 and 6.96 ppm, respectively, consistent with the pyrenyl−anthracene−anthracene−pyrenyl stacking mode in $MCAT_{CBBC}$. The ^{1}H DOSY NMR spectrum (Supplementary Fig. 55) of $MCAT_{CBBC}$ revealed that all of the aromatic proton signals had a single diffusion constant ($D = 5.11 \times 10^{-10}$ m^2 s^{-1}), indicating the presence of only a unique assembly stoichiometry. Moreover, the formation of heteroleptic $MCAT_{CBBC}$ in solution was further confirmed by the ESI mass spectrum, which showed a series of peaks at m/z = 904.9167 (calcd for $[MCAT_{CBBC} - 3(PF_6^-)]^{3+}$ 904.9002) and 1429.8345 (calcd for $[MCAT_{CBBC} - 2(PF_6^-)]^{2+}$ 1429.8326), which is consistent with the theoretical isotopic distributions (Fig. 4h and Supplementary Fig. 56).

Considering the labile nature of the Ag–C_{NHC} bond and the efficient assembly of two-component MCATs from NHC ligands and Ag^{I} ions, we subsequently performed experiments to investigate whether these heteroleptic systems can be formed by the rearrangement of homoleptic assemblies. Indeed, mixing $MCAT_{AAAA}$ and $MCAT_{CCCC}$ at a ratio of 1:1 resulted in rapid (few seconds) conversion to heteroleptic $MCAT_{CAAC}$ (Fig. 2, *method* f), as suggested by the ^{1}H NMR spectrum (Supplementary Fig. 47). Interestingly, although the reaction of the proligand H_2B with Ag_2O produced only the binulear MR_{BB} rather than MCAT, $MCAT_{CCCC}$ and MR_{BB} could still be rapidly converted to $MCAT_{CBBC}$ when it was mixed in CD_3CN at a ratio of 1:2 (Fig. 2, *method* g), as revealed by ^{1}H NMR spectroscopy (Supplementary Fig. 57). These fusion reactions indicate that heteroleptic $MCAT_{CAAC}$ and $MCAT_{CBBC}$, which are selectively formed through integrative self-sorting, represent thermodynamically favorable reaction products.

To investigate whether the structures of $MCAT_{CAAC}$ and $MCAT_{CBBC}$ varied with respect to the concentration and temperature of the solution, concentration dilution and variable-temperature

experiments were subsequently performed. Variable-concentration ^{1}H NMR spectra of $MCAT_{CAAC}$ (Supplementary Fig. 48) and $MCAT_{CBBC}$ (Supplementary Fig. 58) in CD_3CN revealed that only the peak intensities gradually decreased as the concentration was diluted from 6.0 to 0.1 mM, while both the peak count and integral ratios remained largely unchanged. Variable-temperature ^{1}H NMR spectra of $MCAT_{CAAC}$ (Supplementary Fig. 49) and $MCAT_{CBBC}$ (Supplementary Fig. 59) in CD_3CN revealed that the number, shape and chemical shifts of signals changed negligibly over the range of -20~65°C. These observations indicate that both $MCAT_{CAAC}$ and $MCAT_{CBBC}$ can be maintained without structural changes in the acetonitrile solution. Furthermore, NMR titration studies of $MCAT_{CAAC}$ (Supplementary Fig. 50) and $MCAT_{CBBC}$ (Supplementary Fig. 60) revealed that gradually changing the solvent from CD_3CN to DMF-d_7 resulted exclusively continuous shifts of their characteristic proton resonances. These shifts are consistent with expected solvent effects, indicating that both $MCAT_{CAAC}$ and $MCAT_{CBBC}$ maintain their structural integrity in the presence of DMF.

Synthesis and characterization of heteroleptic $MCAT_{CABC}$ with three different di-NHC ligands

We have shown the construction of heteroleptic MCATs (with two different di-NHC ligands) either by a one-pot strategy with Ag_2O and the corresponding individual di-NHC precursors or via catenane–to–catenane transformations from homoleptic precursors. Notably, in contrast to the assembly from the individual ligands, the conversion of homoleptic assemblies to heteroleptic MCATs can be accomplished in a few seconds at room temperature, presumably because no deprotonation step is required in supramolecular fusion.

On the basis of these results, we were interested in whether the structural complexity of the system could be further increased by further fusing two heteroleptic MCATs. We carefully inspected heteroleptic $MCAT_{CAAC}$ and $MCAT_{CBBC}$ and determined that not only do they have the same pyrene-bridged external ligand, but their internal ligands differ by only two atoms. Considering the similarities in the structure and composition of $MCAT_{CAAC}$ and $MCAT_{CBBC}$, we speculated that their fusion can result in heteroleptic MCATs with more sequences. When two

heteroleptic $MCAT_{CAAC}$ and $MCAT_{CBBC}$ were mixed at room temperature at a ratio of 1:1 in CD_3CN (Fig. 2, method h), a complex new set of signals could be observed in the NMR spectra (Fig. 4f and Supplementary Figs. 61–64), indicating the formation of a new assembly through self-sorting, denoted $MCAT_{CABC}$. In addition, the ^1H DOSY NMR spectrum of the reaction mixture revealed that there was a single diffusion coefficient ($D = 5.25 \times 10^{-10}$ m^2 s^{-1}), suggesting that only one stoichiometric group of the assembly formed (Supplementary Fig. 65). The ESI mass data clearly revealed that the product with the formula $[Ag_4(A)(B)(C)_2]$ formed, and the peaks at m/z = 905.5603 and 1430.8234 could be attributed to the $\{MCAT_{CABC} - 3(PF_6^-)\}^{3+}$ and $\{MCAT_{CABC} - 2(PF_6^-)\}^{2+}$ species (Fig. 4i and Supplementary Fig. 66).

Single crystals of the $MCAT_{CABC}$ assembly suitable for SCXRD analysis were obtained by slow diffusion of diethyl ether into the solution (V_{MeCN}/V_{DMSO} = 15:1) of the compound. Notably, SCXRD analysis (Fig. 3d) unambiguously confirmed the MCAT structure of $MCAT_{CABC}$, comprising three distinct di-NHC ligands. We note that this is probably the architecture of MCAT with the highest degree of ligand differentiation and precisely defined structure achieved to date. Moreover, the solid-state structure of the $MCAT_{CABC}$ assembly revealed that one MR_{AC} consists of phenazine-bridged di-NHC ligand A and pyrene-bridged di-NHC ligand C connected by two silver(I) ions, whereas the other MR_{BC} is supported by ligand C and anthracene-bridged ligand B connected by two silver ions. Notably, two pyrene units are located outside the cavity of the two interlocked metallacycles, while anthracene and phenazine units are threaded through the second interlocked metallacycle, resulting in a pyrene–anthracene–phenazine–pyrene parallel arrangement. In the solid structure of $MCAT_{CABC}$, $\pi\cdots\pi$ stacking interactions are observed between the pyrene and anthracene groups with an interplanar distance of 3.4 Å, in addition to donor–acceptor interactions between the phenazine unit and the adjacent pyrene or anthracene group, as inferred from the interring distances of 3.3–3.4 Å. These interactions are the main driving forces for the formation of the interlocked structure.

Further experiments were performed to investigate the stability of heteroleptic $MCAT_{CABC}$ relative to those of the homoleptic $MCAT_{AAAA}$, $MCAT_{CCCC}$, and MR_{BB}. A mixture of $MCAT_{AAAA}$

(1 equiv), MR_{BB} (2 equiv) and $MCAT_{CCCC}$ (2 equiv) was allowed to equilibrate in CD_3CN at room temperature (Fig. 2, method **i**). Analyses of the reaction mixture by ^1H NMR were consistent with the presence of $MCAT_{CABC}$ as the unique product in solution (Supplementary Fig. 67b). Alternatively, treating the H_2A, H_2B and H_2C ligands at a ratio of 1:1:2 with Ag_2O in acetonitrile at 65°C for 12 hours (Fig. 2, method j) resulted in the formation of $MCAT_{CABC,}$ as revealed by ^1H NMR spectroscopy (Supplementary Fig. 67c). These observations indicate that heteroleptic assembly $MCAT_{CABC}$ is the thermodynamically favored reaction product. The stability of the formed heteroleptic $MCAT_{CABC}$ was further investigated. Notably, the number, shapes and chemical shifts of the signals changed negligibly in the ^1H NMR spectra of $MCAT_{CABC}$ either at different concentrations (6.0−0.1 mM) (Supplementary Fig. 68) or at a range of temperatures (−20−65°C) (Supplementary Fig. 69), revealing the stability of the heteroleptic MCAT structure in acetonitrile solution. Moerever, NMR titration studies (Supplementary Fig. 70) indicate that $MCAT_{CABC}$ can also maintained without structural changes in the presence of DMF.

Furthermore, with the visual molecular dynamics (VMD) program[52] and wavefunction software Multifwn 3.8[53], an independent gradient model based on Hirshfeld partition (IGMH) analysis[54,55] revealed three IGMH δg^{inter} isosurfaces corresponding to van der Waals interactions within three heteroleptic MCATs (Supplementary Fig. 71). Both pyrene and phenazine moieties contain π electrons (prerequisite for π···π stacking), the interaction itself stems from dispersion forces between parallel π electron clouds, and the nearly flat shape of the δg^{inter} isosurfaces between π-conjugated fragments is a hallmark feature of π···π stacking[56,57].

Theoretical Study

Unlike MCATs that bear a single type of NHC ligand, those incorporating two or more distinct NHC ligands have different component sequences defined by the arrangement of their ligands. Notably, dimerization of either two identical or two different heteroleptic MRs should yield MCATs with numerous possible sequences. However, the abovementioned experimental results revealed only three specific sequences. To elucidate this selective self-assembly, we conducted theoretical investigations employing semiempirical and DFT calculations.

Beginning with $MCAT_{CAAC}$, we focused on its heteroleptic metalla-rectangle building unit, MR_{AC}. As shown in Fig. 5a, statistical analysis indicated that dimerization of two MR_{AC} units could yield not only $MCAT_{CAAC}$ but also other sequence isomers ($MCAT_{AACC}$ and $MCAT_{ACCA}$). Structures of MR_{AC} and three MCATs were optimized via the semiempirical GFN2-xTB method[58], followed by DFT calculations for single-point energy calculations via the ωB97X-D hybrid functional[59] (Fig. 5c and Supplementary Table 1). The calculated binding energies (E_{BE}s) for the dimerization of the two MR_{AC}s to the MCATs were –387.5 kJ mol^{-1} (for $MCAT_{AACC}$), –306.0 kJ mol^{-1} (for $MCAT_{ACCA}$), and –417.5 kJ mol^{-1} (for $MCAT_{CAAC}$). Comparisons reveal that $MCAT_{CAAC}$ is significantly more stable than $MCAT_{AACC}$ and $MCAT_{ACCA}$ by approximately 30.0 and 111.5 kJ mol^{-1}, respectively. This stability of $MCAT_{CAAC}$ is consistent with experimental observations, indicating that the CAAC component sequence is highly favored during the assembly of MCATs. Similarly, the binding energy E_{BE} (–380.0 kJ mol^{-1}) of $MCAT_{CBBC}$ was substantially greater than that of $MCAT_{BBCC}$ (E_{BE} = –358.0 kJ mol^{-1}) and $MCAT_{BCCB}$ (E_{BE} = –290.1 kJ mol^{-1}), confirming the increased stability of the CBBC component sequence isomer that was observed experimentally (Supplementary Fig. 72 and Table 2).

Next, we extended the theoretical analysis to explain the exclusive experimental observation of $MCAT_{CABC}$ among possible MCATs incorporating three distinct NHC ligands. Unlike the abovementioned cases, $MCAT_{CABC}$ arises from the dimerization of two different heteroleptic metalla-rectangles (MR_{AC} and MR_{BC}). Statistical analysis revealed three other possible sequence isomers, excluding homodimers: $MCAT_{ABCC}$, $MCAT_{BACC}$, and $MCAT_{ACCB}$ (Fig. 5b). Semiempirical optimization and DFT single-point energy calculations (Fig. 5c and Supplementary Table 3) revealed that compared with $MCAT_{ABCC}$ (E_{BE} = –372.6 kJ mol^{-1}), $MCAT_{BACC}$ (E_{BE} = –376.1 kJ mol^{-1}), and $MCAT_{ACCB}$ (E_{BE} = –298.3 kJ mol^{-1}), $MCAT_{CABC}$ has a significantly higher binding energy E_{BE} (–400.3 kJ mol^{-1}). This finding indicates the excellent stability of the CABC component sequence, which is consistent with its exclusive experimental formation.

Near-infrared Photothermal Conversion Study

Although the prevalence of π···π stacking interactions in supramolecular assemblies constitutes a

key stabilization mechanism, it further facilitates nonradiative energy migration and photothermal conversion processes. We have demonstrated that different conjugate planes can be integrated into a single discrete supramolecular assembly by a metal–carbon bond-mediated supramolecular fusion strategy. To reliably determine the effect of different conjugate planes and stacking modes on the photothermal conversion efficiency, the near-infrared photothermal conversion properties of MR_{BB} and five MCATs with different component sequences (AAAA, CCCC, CAAC, CBBC, and CABC) were investigated.

As shown in Fig. 6a and 6b, the three heteroleptic MCATs experienced different and obvious warming processes. Specifically, a solution of $MCAT_{CBBC}$ (1.0 mM in CH_3CN, 1.0 mL) experienced a notable increase in temperature from 22.8 to 37.3°C at 808 nm at 1.5 W cm^{-2}. Intriguingly, a greater temperature increase was detected for $MCAT_{CABC}$ (ΔT = 30.1°C, from 22.4 to 52.5°C) than for $MCAT_{CBBC}$ (ΔT = 14.5°C, from 22.8 to 37.3°C). A 39.7% photothermal conversion efficiency was calculated for $MCAT_{CBBC}$ (Supplementary Fig. 78), and a 46.5% efficiency was calculated for $MCAT_{CABC}$ (Supplementary Fig. 79). Compared with $MCAT_{CBBC}$ and $MCAT_{CABC}$, $MCAT_{CAAC}$ resulted in greater temperature differences (ΔT = 49.3°C, from 23.4 to 72.7°C). According to the equations shown in the ESI, a 79.6% efficiency was calculated for $MCAT_{CAAC}$ (Supplementary Fig. 77). Analysis of the solid-state structures reveals that although all three heteroleptic MCATs have the same number of π···π stacking interactions, compared with $MCAT_{CBBC}$, $MCAT_{CAAC}$ and $MCAT_{CABC}$ exhibit stronger stacking strengths. In addition, in the structure of $MCAT_{CAAC}$, two electron-deficient phenazine skeletons are adjacent to the electron-rich pyrene conjugated groups and arranged in parallel, which is more conducive to electron transport, resulting in a higher photothermal conversion efficiency for $MCAT_{CAAC}$.

In contrast, the solution temperatures of the homoleptic assemblies $MCAT_{AAAA}$, MR_{BB} and $MCAT_{CCCC}$ increased by 28.1°C, 8.6°C, and 13.9°C, respectively (Fig. 6a, 6b and Supplementary Figs. 74–76), which were significantly lower than the temperature increases of the corresponding heteroleptic MCATs. This result further confirms that the near-infrared photothermal conversion performance of the materials can be effectively regulated by changing the ratio and arrangement

of different π-conjugated skeletons in the metalla[2]catenane structure. Furthermore, we recorded the electron paramagnetic resonance (EPR) spectra of MR_{BB} and MCATs. The strong signals indicate the presence of unpaired electrons, which is consistent with the charge-transfer interaction in the ground state. After irradiation, the EPR signals of $MCAT_{AAAA}$, MR_{BB}, $MCAT_{CCCC}$, $MCAT_{CAAC}$, $MCAT_{CBBC}$ and $MCAT_{CABC}$ increased by 12.9, 1.2, 2.4, 16.3, 2.4 and 13.9 times, respectively (Supplementary Figs. 80–85). This observation is consistent with the established conclusion that under 808 nm laser irradiation, the difference in the strong EPR signal with 808 nm laser irradiation of $MCAT_{CAAC}$ indicates its excellent NIR photothermal conversion efficiency.

Discussion

We have demonstrated that heteroleptic metalla-[2]catenanes with stereoscopic layered arrangements provide a versatile platform for exploring how spatial molecular coding guides emergent functions. By selectively constructing sequence-defined assemblies and correlating their structures with thermodynamic stability and photothermal performance, this work establishes a direct link between motif arrangement and system-level properties. In addition to revealing sequence–function relationships in multicomponent assemblies, our findings highlight molecular coding as a guiding principle for the bottom-up design of supramolecular materials.

Extending this strategy to other spatial organizations and functional motifs could enable systematic decoding of molecular information in increasingly complex assemblies. These efforts may uncover new modes of emergent behavior, from electron transport and photonic activity to adaptive mechanical responses. Moreover, embedding coding principles into supramolecular design could reshape how we conceive and engineer functional matter, bridging molecular information with next-generation materials, devices, and energy technologies.

Methods

Synthesis

The ligands H_2A, H_2B and H_2C were synthesized from 2,7-dibromophenazine, 2,6-dibromoanthracene, and 1,6-dibromopyrene, respectively; detailed methods and characterizations

of H_2A, H_2B and H_2C are provided in the Supplementary Information. The homoleptic assemblies $MCAT_{AAAA}$, MR_{BB} and $MCAT_{CCCC}$ were synthesized using Ag_2O and ligands H_2A, H_2B and H_2C, respectively; the heteroleptic assemblies $MCAT_{CAAC}$, $MCAT_{CBBC}$ and $MCAT_{CABC}$ were synthesized either via direct assembly of NHC ligands with Ag(I) nodes or structural transformation from homoleptic precursors trough a supramolecular fusion strategy; detailed methods and characterizations of $MCAT_{AAAA}$, MR_{BB}, $MCAT_{CCCC}$, $MCAT_{CAAC}$, $MCAT_{CBBC}$ and $MCAT_{CABC}$ are provided in the Supplementary Information.

X-ray crystallography

Single crystals of $MCAT_{AAAA}$, $MCAT_{CAAC}$, $MCAT_{CBBC}$ and $MCAT_{CABC}$ suitable for X-ray diffraction were obtained at room temperature. X-ray intensity data for $MCAT_{AAAA}$, $MCAT_{CBBC}$, and $MCAT_{CABC}$ were collected at T = 240 K and those for $MCAT_{CAAC}$ at T = 180 K on a Bruker D8 Venture system and used Mo K_α radiation (λ = 0.71073 Å). Using Olex2[60], the structures were solved with the SHELXT-1997[61,62] structure solution program using direct methods and refined with the SHELXL[63] refinement package using least-squares minimization. All non-hydrogen atoms were refined with anisotropic displacement parameters, and hydrogen atoms were placed in geometrically calculated positions. With these data, the disordered solvent molecules that could not be restrained properly were removed using the SQUEEZE method. The ORTEP-style illustration of four structures can be seen in Supplementary Figures 86 (for $MCAT_{AAAA}$), 87 (for $MCAT_{CAAC}$), 88 (for $MCAT_{CBBC}$) and 89 (for $MCAT_{CABC}$), with probability ellipsoids. Details of the X-ray crystallographic refinement of $MCAT_{AAAA}$, $MCAT_{CAAC}$, $MCAT_{CBBC}$ and $MCAT_{CABC}$ can be found in Supplementary Tables 4, 5, 6 and 7, respectively.

Computational details

The computational study using the combination of self-consistent tight-binding (GFN2-xTB)[58], and density functional theory (DFT) calculations were performed with the Guassian09 quantum chemistry package[64]. The geometries of MRs and MCATs were optimized using semi-empirical GFN2-xTB method implemented with D4 model[65]. The relative stability of feasible supramolecular structures was investigated through single-point calculations using ωB97X-D

hybrid functional[59] with the 6-31G(d,p)[66] basis set for non-metal atoms (C, H, N) atoms and the LANL2DZ[67] basis set for metal atoms (Ag). Acetonitrile was used as a solvent for calculations (SMD model)[68].

Near-infrared photothermal conversion research

To guarantee same amount of conjugated-π area, the applied molar ratio of the six topologies $MCAT_{AAAA}$ / MR_{BB} / $MCAT_{CCCC}$ / $MCAT_{CAAC}$ / $MCAT_{CBBC}$ / $MCAT_{CABC}$ was 1:2:1:1:1:1. Compound $MCAT_{AAAA}$ (9.33 mg, 0.003 mmol) was added into a solvent of CH_3CN (3mL). After the solid dissolved absolutely, 1.0 mL of this solution was taken into a 2.0 mL sample vessel and put into the bright spot of a laser with 808 nm wavelength at 1.5 W/cm^2. Temperature variation of the solution was detected by an infrared camera. Compound MR_{BB} (9.29 mg, 0.006 mmol), compound $MCAT_{CCCC}$ (9.59 mg, 0.003 mmol), compound $MCAT_{CAAC}$ (9.46 mg, 0.003 mmol), compound $MCAT_{CBBC}$ (9.45 mg, 0.003 mmol) and compound $MCAT_{CABC}$ (9.45 mg, 0.003 mmol) were detected with the same procedure as compound $MCAT_{AAAA}$.

Data Availability

The authors declare that all data supporting the findings of this study are available within the article and Supplementary Information files, and are also available from the corresponding author upon request. The X-ray crystallographic coordinates for structures have been deposited at the Cambridge Crystallographic Data Center (CCDC) under deposition numbers CCDC-2483191 ($MCAT_{AAAA}$), CCDC-2483192 ($MCAT_{CAAC}$), CCDC-2483193 ($MCAT_{CABC}$), CCDC-2483194 ($MCAT_{CBBC}$), respectively. These data can be obtained free of charge via http://www.ccdc.cam.ac.uk/data_request/cif. Source Data are provided with this manuscript.

References

1. Lehn, J.-M. Toward complex matter: supramolecular chemistry and self-organization. *Proc. Natl. Acad. Sci. U.S.A.* **99**, 4763−4768 (2002).
2. Konar, M. & Govindaraju, T. *Molecular Architectonics and Nanoarchitectonics* Ch. 1 (Springer Press. , Singapore, 2022).
3. Lee, J. M. *et al.* Semiautomated synthesis of sequence-defined polymers for information storage. *Sci.*

Adv. **8**, eabl8614 (2022).

4. Bielecki, A. & Schmittel, M. The information encoded in structures: theory and application to molecular cybernetics. *Found. Sci.* **27**, 1327−1345 (2022).
5. Wu, K. *et al.* Systematic construction of progressively larger capsules from a fivefold linking pyrrole-based subcomponent. *Nat. Synth.* **2**, 789−797 (2023).
6. Qi, H. *et al.* Steric complementarity drives strong co-assembly of short peptide stereoisomers. *J. Am. Chem. Soc.* **147**, 14231−14243 (2025).
7. Benchimol, E., Nguyen, B.-N. T., Ronson, T. K. & Nitschke, J. R. Transformation networks of metal–organic cages controlled by chemical stimuli. *Chem. Soc. Rev*. **51**, 5101−5135 (2022).
8. McTernan, C. T., Davies, J. A. & Nitschke, J. R. Beyond platonic: how to build metal-organic polyhedra capable of binding low-symmetry, information-rich molecular cargoes. *Chem. Rev.* **122**, 10393−10437 (2022).
9. Levin, A. *et al.* Biomimetic peptide self-assembly for functional materials. *Nat. Rev. Chem.* **4**, 615−634 (2020).
10. Zhu, Y. *et al.* A general strategy for synthesizing biomacromolecular ionogel membranes via solvent-induced self-assembly. *Nat. Synth.* **2**, 864−872 (2023).
11. Wu, H. *et al.* Photocatalytic and photoelectrochemical systems: similarities and differences. *Adv. Mater.* **32**, 1904717 (2020).
12. Ma, B. & Bianco, A. Regulation of biological processes by intrinsically chiral engineered materials. *Nat. Rev. Mater.* **8**, 403−413 (2023).
13. Dong, J., Liu, Y. & Cui, Y. Emerging chiral two-dimensional materials. *Nat. Chem.* **16**, 1398−1407 (2024).
14. Raymond, D. M. & Nilsson, B. L. Multicomponent peptide assemblies. *Chem. Soc. Rev.* **47**, 3659−3720 (2018).
15. Zhu, J. *et al.* Protein assembly by design. *Chem. Rev.* **121**, 13701−13796 (2021).
16. Li, L., Zheng, R. & Sun, R. Understanding multicomponent low molecular weight gels from gelators to networks. *J. Adv. Res.* **69**, 91−106 (2025).
17. Jin, T. *et al.* Exploring self-sorting in metallacycles: toward advanced supramolecular systems and materials. *Supramol. Mater.* **4**, 100117 (2025).
18. Dong, X. Y., Domayer, M., Hudalla, G. A. & Hall, C. K. Modulating peptide co-assembly via macromolecular crowding: recipes for co-assembled structures. *Nanoscale* **17**, 15478−15492 (2025).
19. Cui, H. & Tirrell, M. Self-assembling peptides, conjugates, and mimics: a versatile platform for materials and beyond. *Acc. Chem. Res.* **58**, 163−164 (2025).
20. He, Z., Jiang, W. & Schalley, C. A. Integrative self-sorting: a versatile strategy for the construction of complex supramolecular architecture. *Chem. Soc. Rev.* **44**, 779−789 (2015).
21. Pullen, S. & Clever, G. H. Mixed-ligand metal-organic frameworks and heteroleptic coordination cages

as multifunctional scaffolds—a comparison. *Acc. Chem. Res.* **51**, 3052−3064 (2018).

22. Wu, K., Benchimol, E., Baksi, A. & Clever, G. H. Non-statistical assembly of multicomponent [Pd_2ABCD] cages. *Nat. Chem*. **16**, 584–591 (2024).
23. Fujita, M., Tominaga, M., Hori, A. & Therrien, B. Coordination assemblies from a Pd(II)-cornered square complex. *Acc. Chem. Res.* **38**, 369−378 (2005).
24. Yamashina, M., Yuki, T., Sei, Y., Akita, M. & Yoshizawa, M. Anisotropic expansion of an M_2L_4 coordination capsule: host capability and frame rearrangement. *Chem. Eur. J.* **21**, 4200−4204 (2015).
25. Davies, J. A., Ronson, T. K. & Nitschke, J. R. Triamine and tetramine edge-length matching drives heteroleptic triangular and tetragonal prism assembly. *J. Am. Chem. Soc.* **146**, 5215−5223 (2024).
26. Hou, Y., Zhang, Z. & Zhang, M. Multicomponent metallacages via the integrative self-assembly of Pt(II) nodes with multiple pyridyl and carboxylate ligands. *Acc. Chem. Res.* **58**, 1644−1656 (2025).
27. Northrop, B. H., Zheng, Y.-R., Chi, K.-W. & Stang, P. J. Self-organization in coordination-driven self-assembly. *Acc. Chem. Res.* **42**, 1554−1563 (2009).
28. Han, Y.-F. & Jin, G.-X. Half-sandwich iridium- and rhodium-based organometallic architectures: rational design, synthesis, characterization, and applications. *Acc. Chem. Res.* **47**, 3571−3579 (2014).
29. Sinha, N. & Hahn, F. E. Metallosupramolecular architectures obtained from poly-N-heterocyclic carbene ligands. *Acc. Chem. Res.* **50**, 2167−2184 (2017).
30. Lescop, C. Coordination-driven syntheses of compact supramolecular metallacycles toward extended metallo-organic stacked supramolecular assemblies. *Acc. Chem. Res.* **50**, 885−894 (2017).
31. Zhang, Y.-Y., Gao, W.-X., Lin, L. & Jin, G.-X. Recent advances in the construction and applications of heterometallic macrocycles and cages. *Coord. Chem. Rev.* **344**, 323−344 (2017).
32. Jayamurugan, G., Roberts, D. A., Ronson, T. K. & Nitschke, J. R. Selective endo and exo binding of mono- and ditopic ligands to a rhomboidal diporphyrin prism. *Angew. Chem. Int. Ed.* **54**, 7539−7543 (2015).
33. García-Simón, C. *et al.* Enantioselective hydroformylation by a Rh-catalyst entrapped in a supramolecular metallocage. *J. Am. Chem. Soc.* **137**, 2680−2687 (2015).
34. Chepelin, O., Ujma, J., Barran, P. E. & Lusby, P. J. Sequential, kinetically controlled synthesis of multicomponent stereoisomeric assemblies. *Angew. Chem. Int. Ed.* **51**, 4194−4197 (2012).
35. Preston, D., Barnsley, J. E., Gordon, K. C. & Crowley, J. D. Controlled formation of heteroleptic $[Pd_2(L_a)_2(L_b)_2]^{4+}$ cages. *J. Am. Chem. Soc.* **138**, 10578−10585 (2016).
36. Abe, T., Sanada, N., Takeuchi, K., Okazawa, A. & Hiraoka, S. Assembly of six types of heteroleptic Pd_2L_4 cages under kinetic control. *J. Am. Chem. Soc.* **145**, 28061−28074 (2023).
37. Zhang, D., Ronson, T. K., Zou, Y.-Q. & Nitschke, J. R. Metal–organic cages for molecular separations. *Nat. Rev. Chem.* **5**, 168−182 (2021).
38. Banerjee, R., Chakraborty, D. & Mukherjee, P. S. Molecular barrels as potential hosts: from synthesis to applications. *J. Am. Chem. Soc.* **145**, 7692−7711 (2023).

39. Howlader, P., Das, P., Zangrando, E. & Mukherjee, P. S. Urea-functionalized self-assembled molecular prism for heterogeneous catalysis in water. *J. Am. Chem. Soc.* **138**, 1668−1676 (2016).
40. Jiao, J. *et al.* Design and assembly of chiral coordination cages for asymmetric sequential reactions. *J. Am. Chem. Soc.* **140**, 2251−2259 (2018).
41. Gao, W.-X., Zhang, H.-N. & Jin, G.-X. Supramolecular catalysis based on discrete heterometallic coordination-driven metallacycles and metallacages. *Coord. Chem. Rev.* **386**, 69−84 (2019).
42. Liu, D. *et al.* Molecular co-catalyst confined within a etallacage for enhanced photocatalytic CO_2 reduction. *J. Am. Chem. Soc.* **146**, 2275−2285 (2024).
43. Gan, M.-M. *et al.* Preparation and post-assembly modification of metallosupramolecular assemblies from poly(N-heterocyclic carbene) ligands. *Chem. Rev.* **118**, 9587−9641 (2018).
44. Bai, S. & Han, Y.-F. Metal-N-heterocyclic carbene chemistry directed toward metallosupramolecular synthesis and beyond. *Acc. Chem. Res.* **56**, 1213−1227 (2023).
45. López-Moreno, A. *et al.* Single-walled carbon nanotubes encapsulated within metallacycles. *Angew. Chem. Int. Ed.* **61**, e202208189 (2022).
46. Ibáñez, S., Poyatos, M., & Peris, E. N-heterocyclic carbenes: a door open to supramolecular organometallic chemistry. *Acc. Chem. Res.* **53**, 1401−1413 (2020).
47. Zhang, Y.-W. *et al.* Unravelling the roles of solvophobic effects and π···π stacking interactions in the formation of [2]catenanes featuring di-(N heterocyclic carbene) building blocks. *Angew. Chem. Int. Ed.* **62**, e202312323 (2023).
48. Chang, J.-P. *et al.* Synthesis of a metalla[2]catenane, metallarectangles and polynuclear assemblies from di(N-heterocyclic carbene) ligands. *Angew. Chem. Int. Ed.* **63**, e202409664 (2024).
49. Zhang, Y.-W., Bai, S., Wang, Y.-Y. & Han, Y.-F. A strategy for the construction of triply interlocked organometallic cages by rational design of poly-NHC precursor. *J. Am. Chem. Soc.* **142**, 13614–13621 (2020).
50. Gao, X. *et al.* Synthesis and near-infrared photothermal conversion of discrete supramolecular topologies featuring half-sandwich [Cp*Rh] units. *J. Am. Chem. Soc.* **143**, 17833−17842 (2021).
51. Wang, Y.-S., Feng, T., Wang, Y.-Y., Hahn, F. E. & Han, Y.-F. Homo- and heteroligand poly-NHC metal assemblies: synthesis by narcissistic and social self-sorting. *Angew. Chem. Int. Ed*. **57**, 15767–15771 (2018).
52. Humphrey, W., Dalke, K. & Schulten, A. VMD: visual molecular dynamics. *J. Mol. Graphics*,**14**, 33–38 (1996).
53. Lu, T. & Chen, F. Multiwfn: A multifunctional wavefunction analyzer. *J. Comput. Chem*. **33**, 580–592 (2012).
54. Lu, T. & Chen, Q. Independent gradient model based on hirshfeld partition: a new method for visual study of interactions in chemical systems. *J. Comput. Chem*. **43**, 539–555 (2022).
55. Lu, T. & Chen, Q. *Comprehensive Computational Chemistry* Vol. 2 (Elsevier Press, Oxford, 2024).

56. Liu, Z. *et al.* Molecular assembly with a figure-of-eight nanohoop as a strategy for the collection and stabilization of cyclo[18]carbon. *Phys. Chem. Chem. Phys*. **25**, 16707–16711 (2023).
57. Liu, Z., Lu, T. & Chen, Q. Intermolecular interaction characteristics of the all-carboatomic ring, cyclo[18]carbon: focusing on molecular adsorption and stacking. *Carbon* **171**, 514–523 (2021).
58. Bannwarth, C., Ehlert, S. & Grimme, S. GFN2-xTB—an accurate and broadly parametrized self-consistent tight-binding quantum chemical method with multipole electrostatics and density-dependent dispersion contributions. *J. Chem. Theory Comput*. **15**, 1652−1671 (2019).
59. Chai, J.-D. & Head-Gordon, M. Long-range corrected hybrid density functionals with damped atom–atom dispersion corrections. *Phys. Chem. Chem. Phys.* **10**, 6615–6620 (2008).
60. Dolomanov, O. V., Bourhis, L. J., Gildea, R. J., Howard, J. A. K. & Puschmann, H. OLEX2: a complete structure solution, refinement and analysis program. *J. Appl. Crystallogr.* **42**, 339–341 (2009).
61. Sheldrick, G. Phase annealing in SHELX-90: direct methods for larger structures. *Acta Crystallogr. A* **46**, 467–473 (1990).
62. Sheldrick, G. A short history of SHELX. *Acta Crystallogr. A* **64**, 112–122 (2008).
63. Sheldrick, G. SHELXT—integrated space-group and crystal-structure determination. *Acta Crystallogr. A* **71**, 3–8 (2015).
64. Gaussian 09 rev. E01 (Gaussian, Inc., 2009). http://www.gaussian.com.
65. Caldeweyher, E. *et al*. A generally applicable atomic-charge dependent London dispersion correction. *J. Chem. Phys*. **150**, 154122 (2019).
66. Hariharan, P. C. & Pople, J. A. The influence of polarization functions on molecular orbital hydrogenation energies. *Theor. Chim. Acta.* **28**, 213–222 (1973).
67. Hay, P. J. & Wadt, W. R. Ab initio effective core potentials for molecular calculations. Potentials for K to Au including the outermost core orbitals. *J. Chem. Phys*. **82**, 299–310 (1985).
68. Marenich, A. V., Cramer, C. J. & Truhlar, D. G. Universal solvation model based on solute electron density and on a continuum model of the solvent defined by the bulk Dielectric constant and atomic surface tensions. *J. Phys. Chem. B* **113**, 6378–6396 (2009).6620

Acknowledgements

The authors gratefully acknowledge financial support from the National Natural Science Foundation of China (22025107 (Y.-F.H.), 92461302 (Y.-F.H.), 22305190 (X.L.), 22301040 (H.-N.Z.)), the National Youth Topnotch Talent Support Program of China (Y.-F.H.), the China Postdoctoral Fellowship Program Grade A (BX20240288 (Y.-W.Z.)), the Shaanxi Postdoctoral Science Foundation Project (2024BSHSDZZ057 (Y.-W.Z.)), the Xi'an Key Laboratory of

Functional Supramolecular Structure and Materials, and the FM&EM International Joint Laboratory of Northwest University.

Author Contributions

Y.-F.H. conceived and supervised the project. Y.-W.Z. and H.-N.Z. performed the synthesis of ligands and silver(I)-N-heterocyclic carbene assemblies. Y.-W.Z., H.-N.Z., M.-X.W., and X.L. performed NMR analyses, X-ray crystallographic analysis, electrospray ionization mass spectrometry, theoretical study and near-infrared photothermal conversion study. Y.-W.Z., H.-N.Z. and Y.-F.H. wrote the paper. All authors contributed to the data analysis and discussion.

Competing Interests

The authors declare no competing interests.

Figure Legends:

Figure 1. Schematic presentation for three arrangements of different motifs and relative sequences in supramolecular architectures. a Radial arrangement of different motifs in metallocages. **b** Circular arrangement of different functional motifs in metallacycles. **c** Stereoscopic layered arrangement of different motifs in tetranuclear NHC MCAT. **d** Two-component MCATs based on four NHC ligands with 8 component sequences. **e** Three-component MCATs based on four NHC ligands with 18 component sequences. *x*, *y*, and *z* were used to denote the numbers of the three NHC ligands. B, G, R, and Y were the capital letters of blue, green, red, and yellow, which were used to denote different building blocks. *x*, *y*, and *z* were used to denote the numbers of the three NHC ligands.

Figure 2. Self-assembly of MCATs from di-NHC ligands H_2A, H_2B and H_2C and structural transformations of the assemblies. **a**–**c** Synthesis of $MCAT_{AAAA}$, MR_{BB} and $MCAT_{CCCC}$ through the reaction of H_2A, H_2B and H_2C, respectively, with Ag_2O in MeCN at 65°C. **d**, **e** Synthesis of $MCAT_{CAAC}$ and $MCAT_{CBBC}$ through the reaction of H_2C and H_2A or H_2B, respectively, in a 1:1 ratio with Ag_2O in acetonitrile at 65°C. **f**, **g** Supramolecular fusion-based transformation of $MCAT_{CCCC}$ and $MCAT_{AAAA}$ or MR_{BB} at a 1:1 ratio or 1:2 ratio to $MCAT_{CAAC}$ and $MCAT_{CBBC}$, respectively, in MeCN at r.t.. Preparation of $MCAT_{CABC}$ through three alternative routes: **h** Reaction of $MCAT_{CAAC}$ and $MCAT_{CBBC}$ in a 1:1 ratio in MeCN at r.t.. **i** Reaction of $MCAT_{AAAA}$, MR_{BB} and $MCAT_{CCCC}$ in a 1:2:2 ratio in MeCN at r.t.. **j** Reaction of H_2A, H_2B and H_2C in a 1:1:2 ratio with Ag_2O in

MeCN at 65°C.

Figure 3. X-ray crystal structures of homoleptic and heteroleptic multicomponent MCATs with one, two or three different ligands. Molecular structure of $MCAT_{AAAA}$ (**a**), $MCAT_{CAAC}$ (**b**), $MCAT_{CBBC}$ (**c**) and $MCAT_{CABC}$ (**d**). From left to right: stick representation, space-filling representation, stacking of ligand backbones, and components of the monomeric binuclear macrocycle. Hydrogen atoms, anions and solvents are omitted for clarity. Three letters (A, B, and C) in the space-filling representation are used to denote phenazine-, anthracene-, and pyrene-based building blocks, respectively.

Figure 4. NMR spectroscopy and ESI mass analysis. Partial ^{1}H NMR spectra (CD_3CN, 400 MHz, 298 K) of (**a**) H_2A, (**b**) H_2B, (**c**) H_2C, (**d**) $MCAT_{CAAC}$, (**e**) $MCAT_{CBBC}$ and (**f**) $MCAT_{CABC}$. Experimental (top, blue) and theoretical (bottom, red) ESI mass spectra of $[MCAT_{CAAC} - 3(PF_6)]^{3+}$ and $[MCAT_{CAAC} - 2(PF_6)]^{2+}$ (**g**), $[MCAT_{CBBC} - 3(PF_6)]^{3+}$ and $[MCAT_{CBBC} - 2(PF_6)]^{2+}$ (**h**), and $[MCAT_{CABC} - 3(PF_6)]^{3+}$ and $[MCAT_{CABC} - 2(PF_6)]^{2+}$ (**i**).

Figure 5. Schematic presentation for the formation of MCATs from two MRs, and semiempirical and DFT calculations analysis. a Statistical outcome of three MCATs with different component sequences (AACC, ACCA, and CAAC) via the dimerization of two identical heteroleptic MRs. **b** Statistical outcome (excluding the narcissistic self-sorting) of four MCATs with different component sequences (ABCC, BACC, ACCB, and CABC) via the assembly of two distinct heteroleptic MRs. **c** Computational study of the relative stabilities of seven feasible MCATs via the GFN2-xTB method (for optimized structures of $MCAT_{AACC}$, $MCAT_{ACCA}$, $MCAT_{CAAC}$, $MCAT_{ABCC}$, $MCAT_{BACC}$, $MCAT_{ACCB}$, and $MCAT_{CABC}$) with DFT calculations for single-point calculations of seven optimized structures using ωB97X-D hybrid functional with the 6-31G(d,p) basis set for non-metal atoms (C, H, N) atoms and the LANL2DZ basis set for metal atoms (Ag).

Figure 6. NIR photothermal conversion analysis. a NIR thermal images of five MCATs with different component sequences (AAAA, CCCC, CAAC, CBBC, and CABC) and MR_{BB} under 808 nm laser irradiation. **b** Photothermal conversion curves of the six topologies. **c** Absorption in the near-infrared region of the six topologies (λ = 700 to 900 nm), the UV−vis absorption spectra (λ = 300 to 900 nm) was shown in Supplementary Figure 73.

Editorial Summary:

Molecular information encoded within supramolecular frameworks offers a powerful paradigm for directing emergent function beyond the genetic code, but systematic investigations into alternative spatial configurations and their consequences remain scarce. Here the authors use metalla-[2]catenanes to probe sequence–function relationships in layered architectures.

Peer review information: *Nature Communications* thanks Mandeep Chahal, Jun-Hua Wan and the other, anonymous, reviewer(s) for their contribution to the peer review of this work. A peer review file is available.

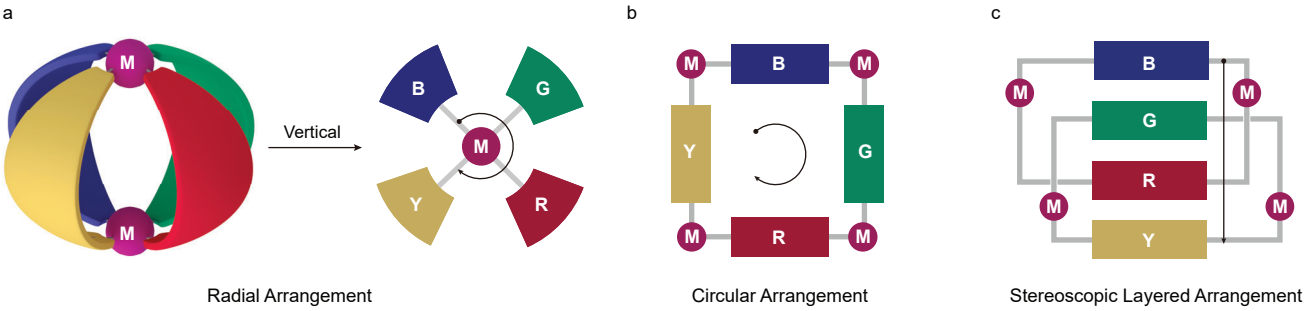

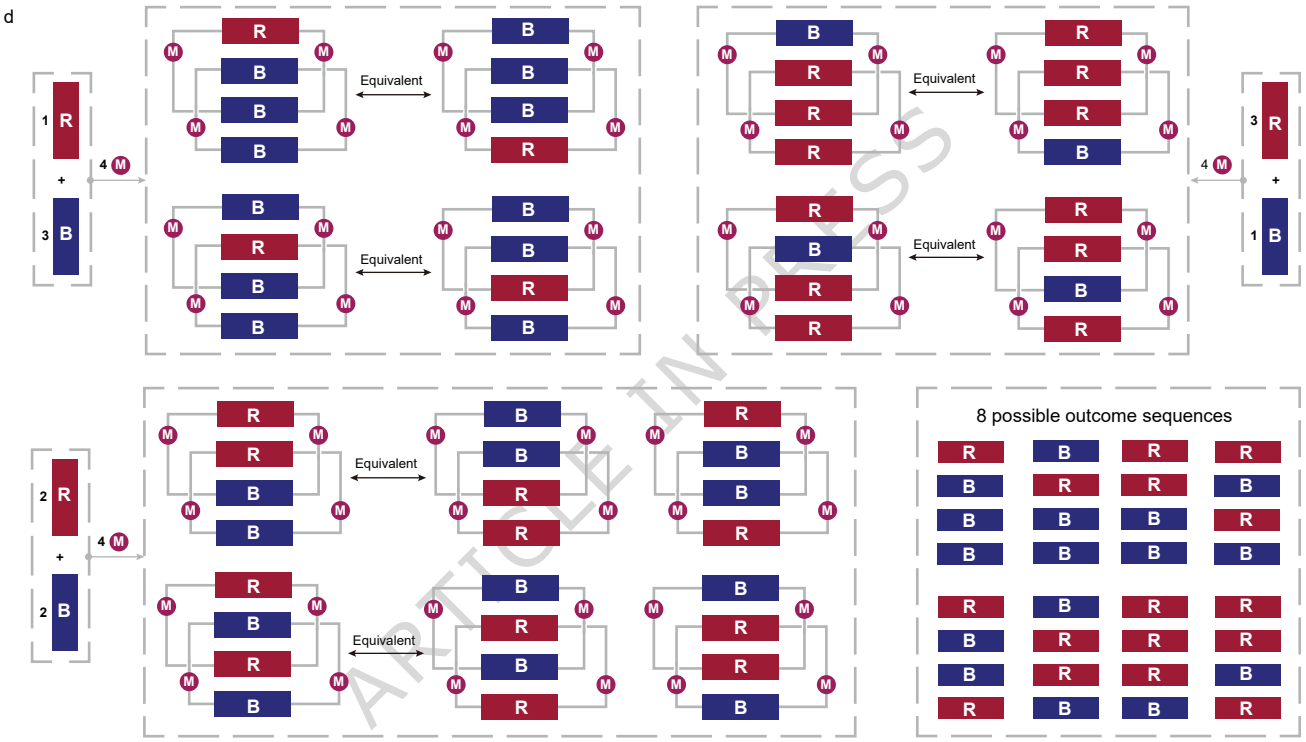

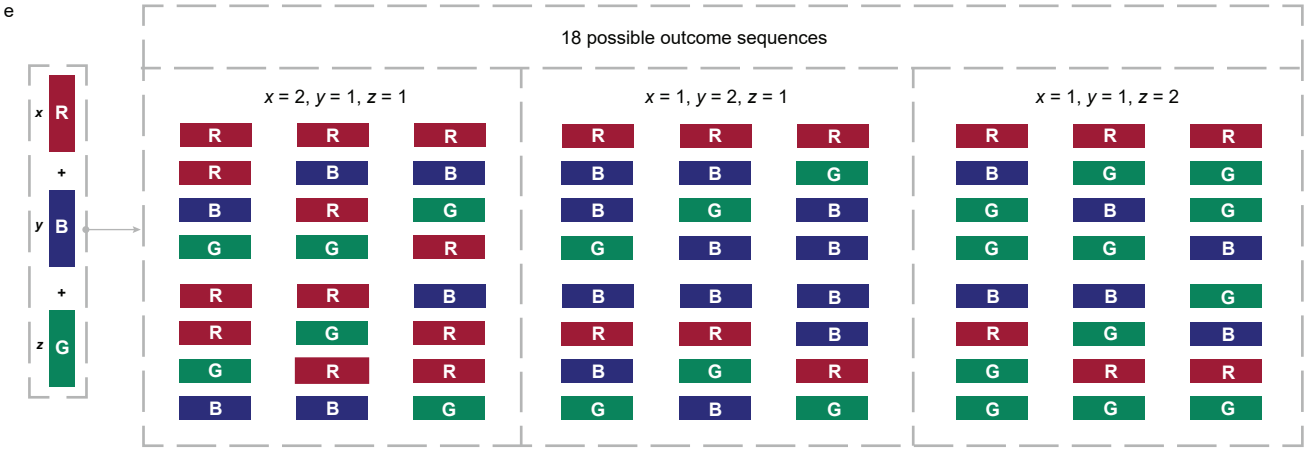

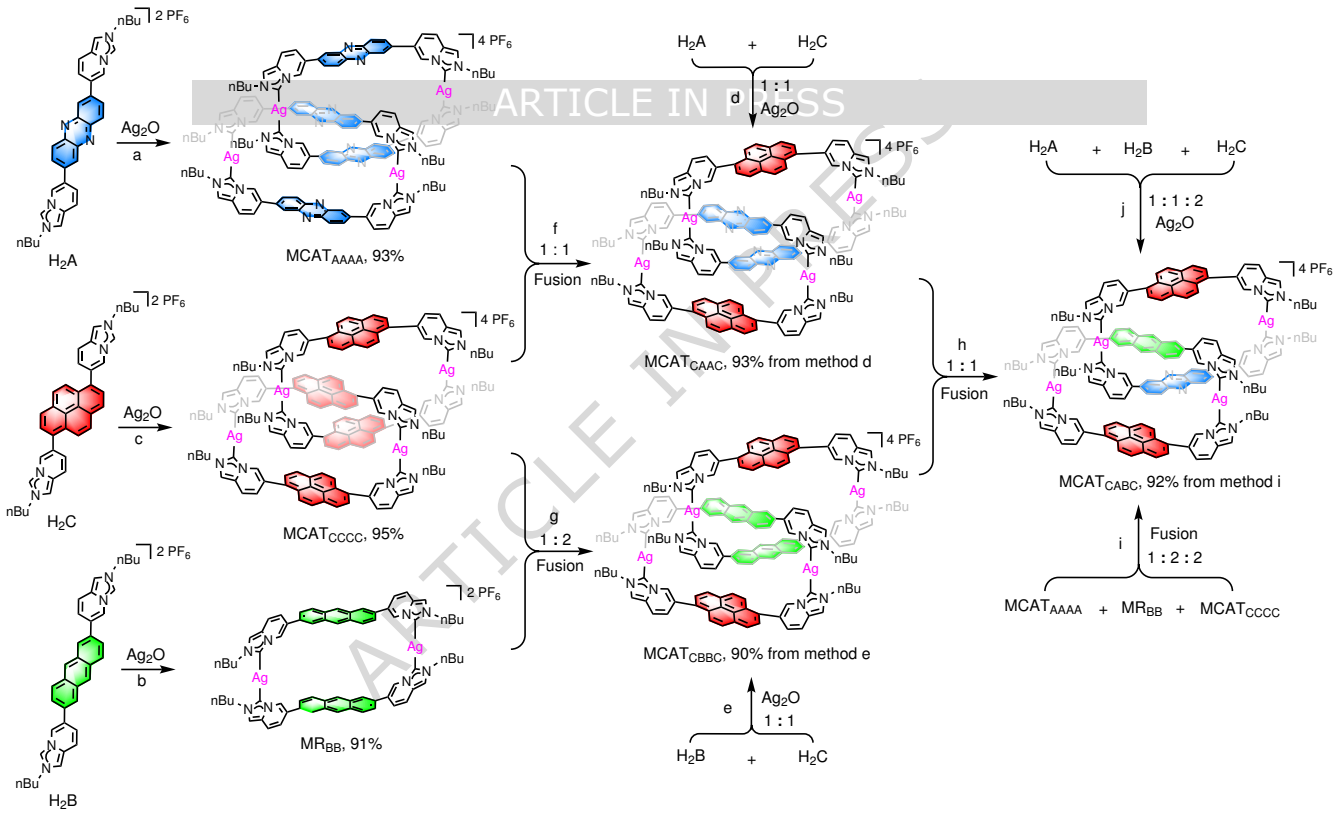

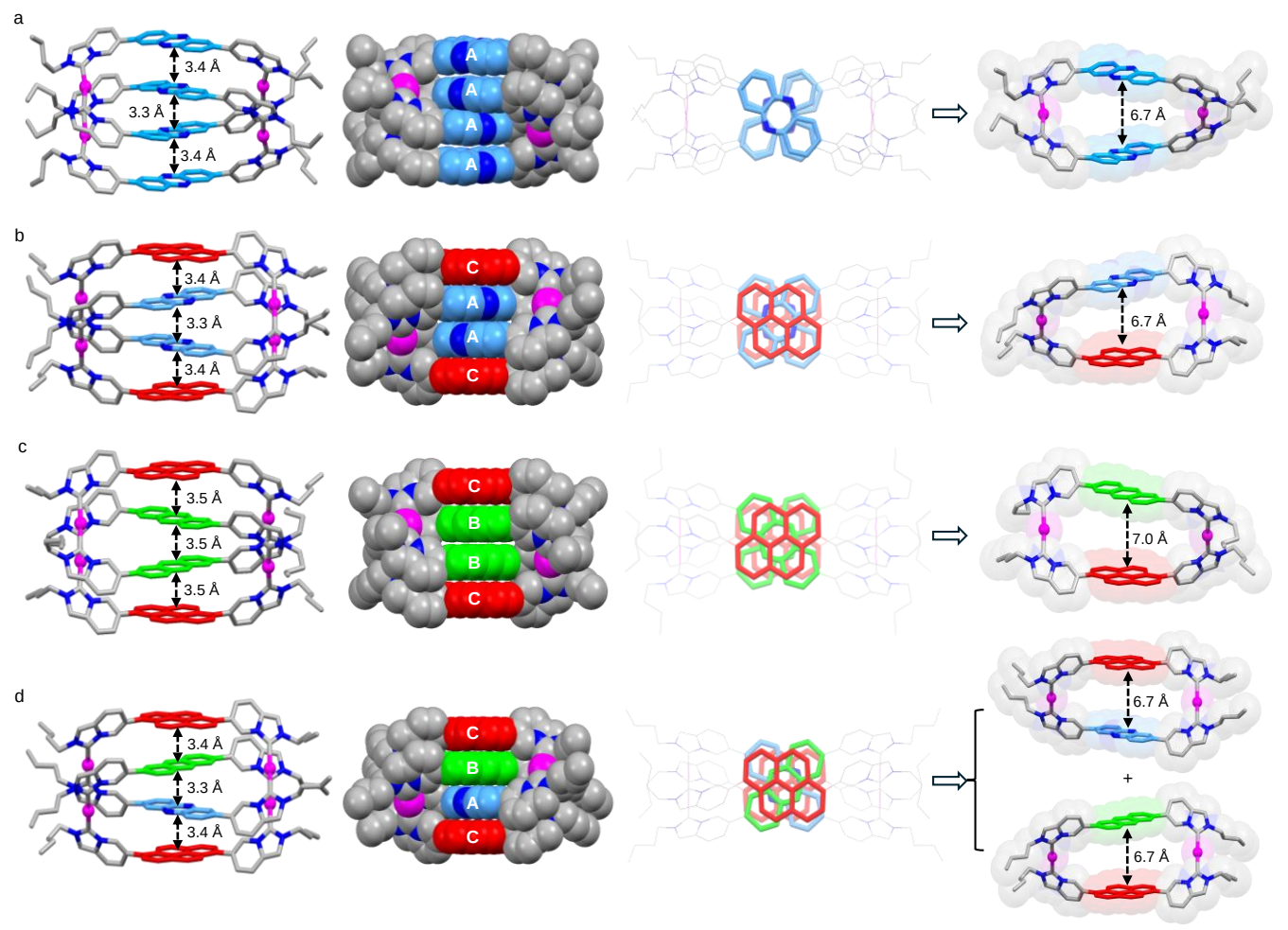
a
3.4 Å
3.3 Å
3.4 Å
A
A
A
A
6.7 Å
b
3.4 Å
3.3 Å
3.4 Å
C
A
A
C
6.7 Å
c
3.5 Å
3.5 Å
3.5 Å
C
B
B
C
7.0 Å
d
3.4 Å
3.3 Å
3.4 Å
C
B
A
C
6.7 Å
+
6.7 Å

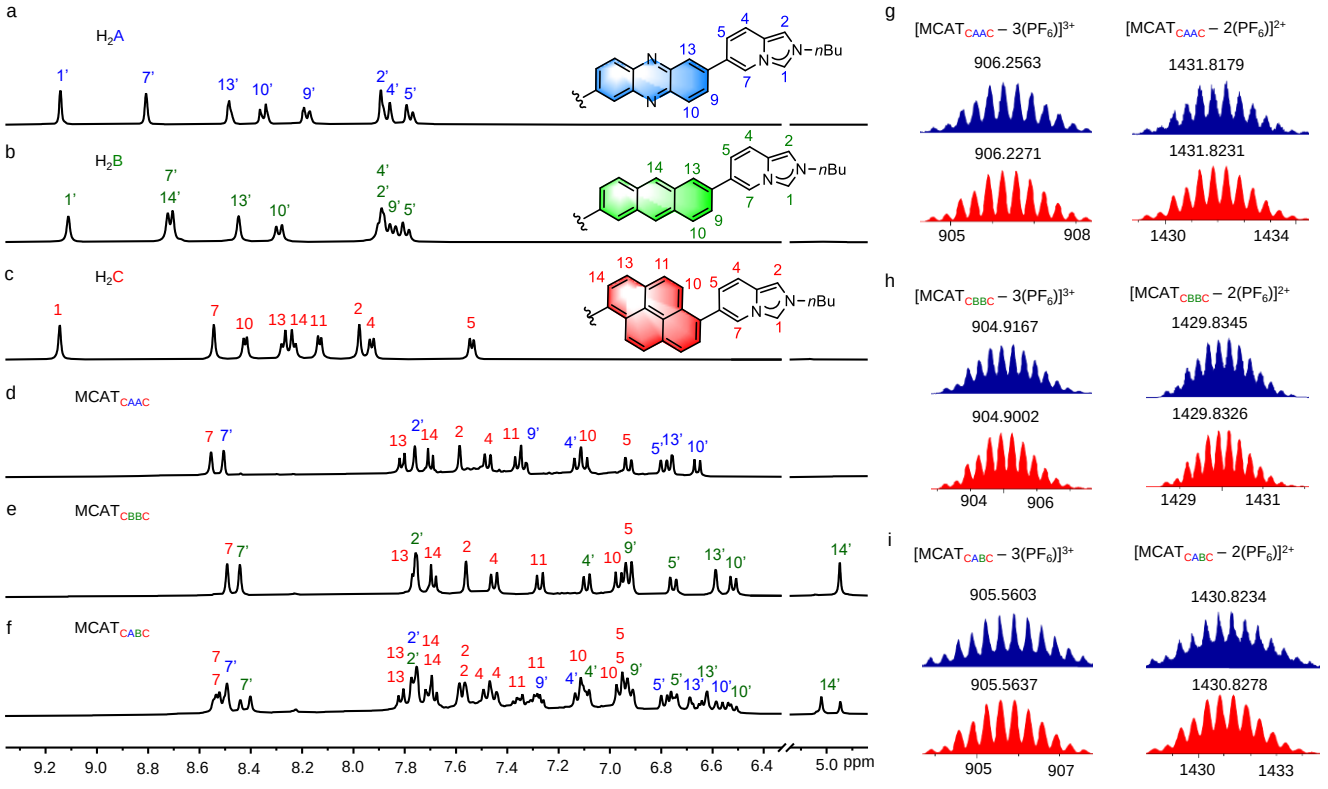
a
H2A
1' 7' 13' 10' 9' 2' 4' 5'
b
H2B
1' 7' 14' 13' 10' 4' 2' 9' 5'
c
H2C
1 7 10 13 14 11 2 4 5
d
MCATCAAC
7 7' 13 2' 14 2 4 11 9' 4' 10 5 5' 13' 10'
e
MCATCBBC
7 7' 13 2' 14 2 4 11 4' 10 5 9' 5' 13' 10' 14'
f
MCATCABC
7 7' 7' 13 13 2' 2' 14 14 2 2 4 4 11 11 9' 10 4' 4' 10 5 5 9' 5' 5' 13 13' 10' 10' 14'
9.2 9.0 8.8 8.6 8.4 8.2 8.0 7.8 7.6 7.4 7.2 7.0 6.8 6.6 6.4 5.0 ppm
N-nBu
g
[MCATCAAC – 3(PF6)]3+
906.2563
906.2271
905 908
[MCATCAAC – 2(PF6)]2+
1431.8179
1431.8231
1430 1434
h
[MCATCBBC – 3(PF6)]3+
904.9167
904.9002
904 906
[MCATCBBC – 2(PF6)]2+
1429.8345
1429.8326
1429 1431
i
[MCATCABC – 3(PF6)]3+
905.5603
905.5637
905 907
[MCATCABC – 2(PF6)]2+
1430.8234
1430.8278
1430 1433

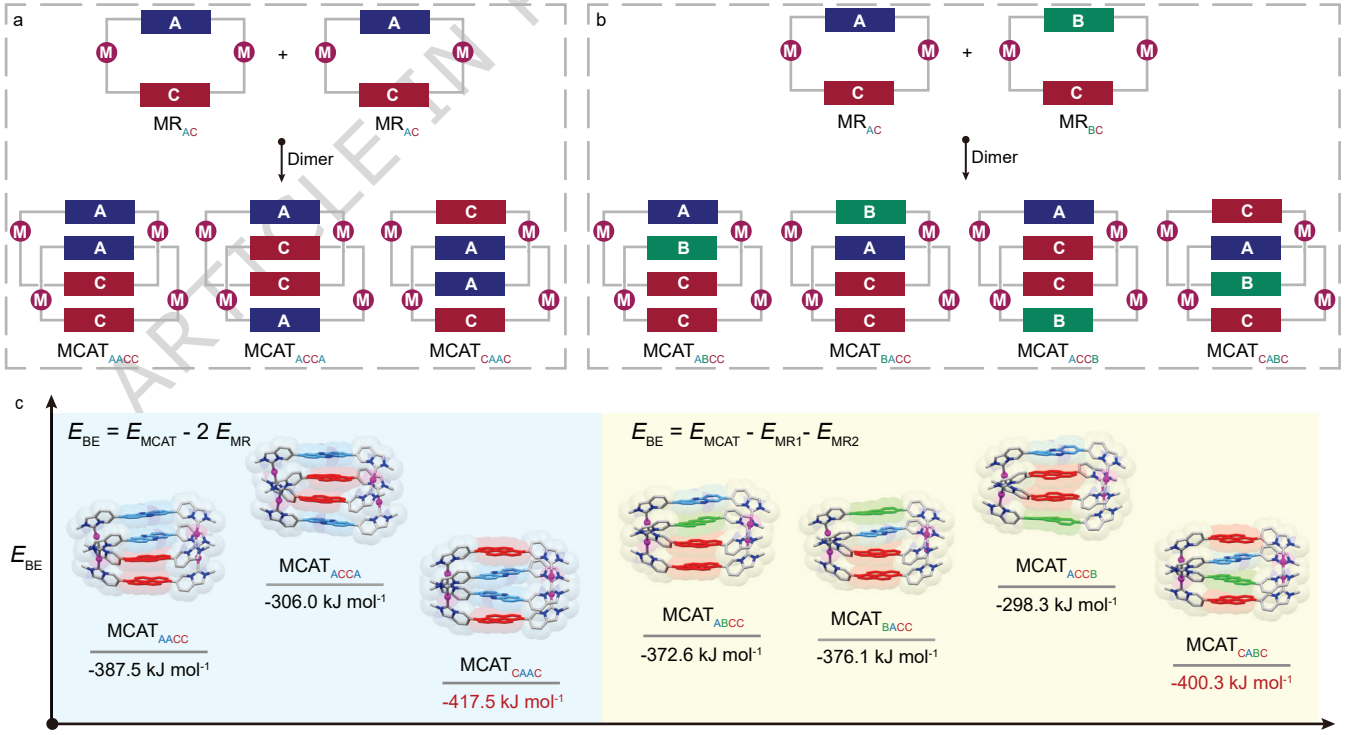

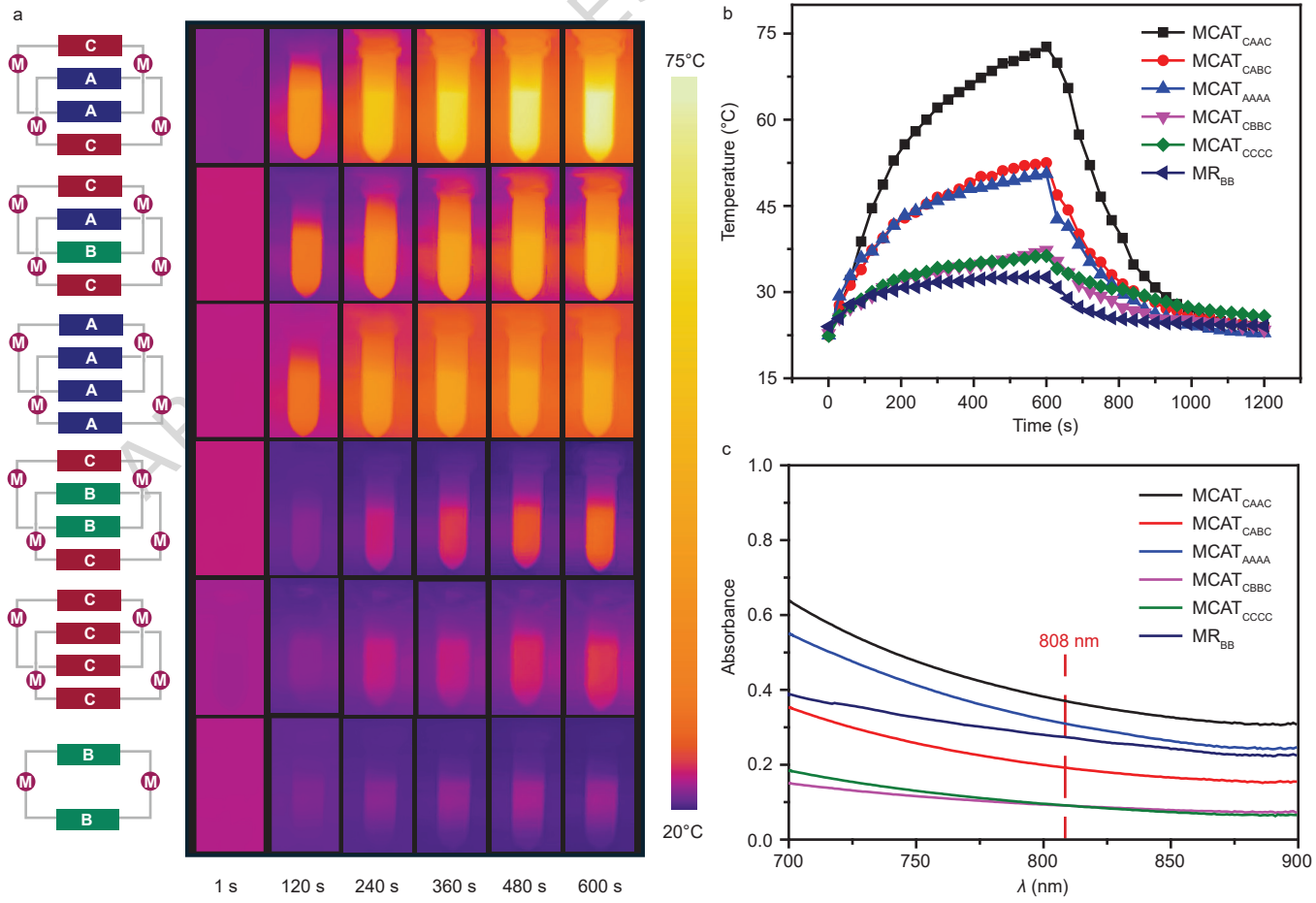
a
C
A
A
C
C
A
B
C
A
A
A
A
C
B
B
C
C
C
C
C
B
B
1 s
120 s
240 s
360 s
480 s
600 s
75°C
20°C
b
MCAT$_{CAAC}$
MCAT$_{CABC}$
MCAT$_{AAAA}$
MCAT$_{CBBC}$
MCAT$_{CCCC}$
MR$_{BB}$
Temperature (°C)
Time (s)
c
Absorbance
808 nm
λ (nm)